
Volumes 178–179, May 2010
ISSN 0368-2048
ELSEVIER
JOURNAL OF
ELECTRON
SPECTROSCOPY
AND
RELATED PHENOMENA
Special Issue:
Trends in X-ray Photoelectron Spectroscopy of solids
(theory, techniques and applications)
Guest Editor:
László Kövér
Journal HomePage: www.elsevier.com/locate/elspec
Available online at
ScienceDirect
www.sciencedirect.com

Journal of Electron Spectroscopy and Related Phenomena 178–179 (2010) 292–302

Contents lists available at ScienceDirect

Journal of Electron Spectroscopy and Related Phenomena

journal homepage: www.elsevier.com/locate/elspec

Review

Structure determination of nanocomposites through 3D imaging using laboratory XPS and multivariate analysis

K. Artyushkova*

Chemical and Nuclear Engineering Department, University of New Mexico, Albuquerque, NM 87131, USA

ARTICLE INFO

Article history:
Available online 29 May 2009

Keywords:
X-ray photoelectron imaging
Multivariate analysis
3D imaging
Image fusion
Peak shape analysis
Depth profiling

ABSTRACT

The purpose of this review is to introduce current trends and future directions in efforts to obtain 3D images of materials both destructively and non-destructively by means of X-ray photoelectron spectroscopy. Non-destructive methods for creating a 3D volume of the material include peak shape analysis, image fusion of angle-resolved images, combination of ARXPS and mapping and multivariate analysis of ARXPS data. Destructive sputtering of nanocomposite samples with ion beams followed by analysis with X-ray photoelectron spectroscopy represents a powerful strategy for in-depth characterization of complex materials. The combination of photoelectron imaging with depth profiling to create 3D images is essential for accurate structure determination of laterally and vertically heterogeneous materials. There are only a few reports in the scientific literature, however, describing this approach. Advances towards realization of these experiments with assistance of multivariate analysis will be discussed.

Contents

1. Introduction 292
2. Review of instrumental capabilities 293
    2.1. Spatial localization 293
    2.2. Destructive depth profiling 293
    2.3. Angle-resolved XPS 294
3. Review of current approaches to generate 3D images of heterogeneous samples 294
    3.1. Conventional approach 294
    3.2. 3D imaging using peak shape analysis algorithm 294
        3.2.1. Tougaard algorithm 294
        3.2.2. MVA/modeling inelastic background 294
    3.3. XPS mapping using automatic ARXPS 295
    3.4. 3D imaging using angle-resolved imaging 296
    3.5. 3D analysis using PARAFAC applied to ARXPS data 298
    3.6. Comparison of methods 299
4. Future directions 299
    4.1. Multivariate analysis of 3D imaging data 299
    4.2. Polyatomic guns for analysis of biological soft samples 300
    Acknowledgements 301
    References 301

1. Introduction

For heterogeneous samples, the concentration variations and local regions of analyte concentration are more important for an understanding of the behavior of complex systems than average composition. XPS imaging and small area spectroscopy provide this important information in lateral dimension, allowing for

---

* Tel.: +1 505 277 0750.
E-mail address: kartyush@unm.edu.

0368-2048/$ – see front matter © 2009 Elsevier B.V. All rights reserved.
doi:10.1016/j.elspec.2009.05.014

a correlation of micro- and macro-scale materials properties. Probing vertical structures is equally important for nanocomposite materials with multiple layers and concentration gradients. X-ray photoelectron spectroscopy offers both destructive and non-destructive means of obtaining quantitative three-dimensional information on chemistry of materials.

The sputtering of solids with ion beams followed by analysis with photoelectron spectroscopy has been widely used as it offers a powerful strategy for the in-depth characterization of complex inorganic materials [1–4]. The combination of imaging techniques with depth profiling to create three-dimensional information is an obvious and exciting extension of these experiments.

The combination of sputtering capabilities and high lateral resolution in images led to the wide spread use of three-dimensional imaging studies using TOF-SIMS [5,6]. The driving force for wide application of this approach has been the development of new sources, such as cluster and polyatomic sources, which allow more controlled removal of material with smaller ion damage and fewer topographic effects which complicate image acquisition [6–11]. A comprehensive three-dimensional microanalysis procedure using a combined scanning electron microscope (SEM)/focused ion beam (FIB) system equipped with an energy-dispersive X-ray spectrometer (EDS) has been developed [12]. The FIB system is used to prepare a site-specific region for X-ray microanalysis followed by the acquisition of an electron-beam generated X-ray spectral image. Serial sectioning procedure can be repeated multiple times to sample a volume of material.

Even though XPS offers very similar capabilities in combining ion sputtering and imaging, there are only a handful number of studies combining XPS imaging and depth sputtering. For example, depth information of coating of a hard disk was obtained by using argon ions beam for etching and subsequent XPS image acquisition in one of these studies [13].

One of the biggest problems when dealing with 3D imaging data sets is visualizing the lateral distribution of chemical moieties as a function of depth. At each depth layer, multiple images can be obtained representing either individual or multiple chemical constituents of nanocomposites. As a simple visualization of lateral distribution as a function of depth, images acquired at selected binding energy (BE) can be combined into a volume and visualized. In addition, multiple stacks of photoelectron images obtained at specific BEs can be overlaid in multiple colors. This approach, however, does only represent chemical species contributing to selected BEs, so that the overall chemistry of different layers may be overlooked.

Similar problem of visualizing and interpreting large data sets is addressed by the application of multivariate analytical (MVA) techniques to multispectral imaging XPS data sets. MVA reduces the dimensionality of the data sets, thereby simplifying data processing, and also improves the signal/noise, so reducing the time required for acquisition [14–17]. Multivariate analysis methods applied to multispectral imaging data sets allow obtaining spatially resolved, quantified, chemical state information.

When multispectral images are acquired at each sputtered depth, four-dimensional data sets can result with a full spectrum acquired at each voxel of the space. These data sets represent a huge amount of data which can only be interpreted with assistance of multivariate analysis [14,18,19].

With the assistance of multivariate analysis, the imaging capability of TOF-SIMS, generates even more useful data, showing distribution of various chemical phases as a function of depth [20]. Four-dimensional spectral image generated by SEM/FIB/EDS analysis was analyzed with Sandia's automated X-ray spectral image analysis software [12]. The component images extracted from MSA, which show the spatial distribution of the various chemical components, were visualized individually or together representing an overall chemistry of individual layers.

This review discusses current approaches in generating 3D images of depth distributions of atoms in the outermost few nanometers and subsurface region of the sample by means of (i) image fusion of angle-resolved imaging, (ii) peak shape analysis in multispectral imaging data sets, (iii) combination of mapping and ARXPS capabilities and (iv) application of multivariate analysis to multispectral and angle-resolved XPS (ARXPS) data. Trends and approaches towards extending application of multivariate analysis to XPS imaging data sets obtained through depth sputtering will also be discussed.

2. Review of instrumental capabilities

2.1. Spatial localization

Different manufacturers of imaging XPS systems have adopted different strategies for obtaining spatial localization—including (1) localization of the probe, by focusing the incident X-rays, (2) localization by limiting area of analysis and (3) use of array detectors with associated imaging optics.

Spatial localization can be achieved by focusing the probe so that it interacts with only a small region of the surface. In order to carry out surface mapping, either the probe must be scanned across the surface, or the surface must be transferred under the probe beam. Thermo's Theta Probe [21], Jeol *JPS-9200* [22] and PHI *Quantera* Scanning X-ray Microprobe [23] are among instruments employing this approach. Neutral particles such as X-ray photons are not readily focused. *JPS-9200* has a minimum X-ray spot size of 30 μm, while *Quantera*'s unique scanning X-ray source with 9 μm diameter minimum X-ray beam size provides the best micro-area spectroscopy performance [23]. The ability to map very large areas is achieved with this approach. Thermo's *Theta Probe*, for example, provides high throughput mapping of up to 70 mm × 70 mm areas [21].

The alternative approach is to expose a large area of the sample to the probe and to collect signal from only a small region of the sample. In this instance, the spatial localization is occurring on the detection side of the technique. In order to gets an image of the surface using a single detector it is necessary to either scan the sample underneath the detection system or use additional scanning plates in the electron-optical focusing system. Exceptional small spot capabilities (<15 μm) in Kratos instruments, for example, are achieved via a series of selected area apertures used in combination with the magnetic and electrostatic lenses [24].

The third approach to obtaining images involves employing a linear array or two-dimensional array of detecting elements. In this type of system, the emission from different parts of the surface is effectively focused onto different parts of the array detector. In parallel imaging mode of Kratos instruments photoelectrons are transferred to the spherical mirror analyzer to produce real time chemical state images with spatial resolution of less than 3 μm [24]. *ESCALAB 250* by Thermo VG provides parallel images with a resolution of about 1 μm [25]. New Omicron *NanoESCA* provides unique lateral resolution in imaging ESCA of 650 nm in the laboratory and 150 nm with Synchrotron source [26]. Its patented design includes a non-magnetic, electrostatic PEEM lens and a double-pass hemispherical analyzer. Use of cathode lens in *NanoESCA*, however, makes analysis of insulators difficult.

2.2. Destructive depth profiling

All modern spectrometers are equipped with Ar sputter ion guns for thin film depth profiling. Recently, developed polyatomic guns are offered now by Phi (C_{60} gun) [27] and by Kratos (Coronene gun) [28]. This development offers capabilities in quantifying the chemical and molecular gradients in the near surface region of soft materials, such as polymers and biomaterials while maintaining molecular integrity.

2.3. Angle-resolved XPS

In the majority of modern spectrometers, angle-dependent spectroscopic and imaging data are acquired by tilting the sample with respect to the analyzer. To obtain ARXPS data, the angular acceptance of the transfer lens should be set to provide good angular resolution. Thermo VG Scientific Theta has a capability to provide angular data simultaneously without tilting the sample. This instrument records spectra over the range of emission angles from 23° to 83° simultaneously. The spectra may be recorded at 0.625° angular intervals [21]. The 2D detector at the output plane has photoelectron energy dispersed at one direction and the angular distribution dispersed in the other direction. This approach allows measurements be taken from very large specimens, which are too large to be tilted, and ensures constant analysis position and area during analysis.

3. Review of current approaches to generate 3D images of heterogeneous samples

3.1. Conventional approach

Gao et al. were among the first who published the combination of XPS imaging with depth profiling [13]. They used argon ion beam and imaging XPS to determine the depth information of coating of a hard disk. A set of elemental images was then displayed and qualitatively analyzed individually at each sputtered depth of interest. In addition, the thickness of each layer was obtained by measuring the depth distribution of an element, which only exists in that specific layer. The etching rate for each layer was calculated by the transport of ions in matter (TRIM) simulation. The etching time for each layer was calculated and finally the thickness of layers was measured. As discussed in Section 1, this approach, however, is limited to images selected by the analyst and does not provide an overall chemistry.

3.2. 3D imaging using peak shape analysis algorithm

Several approaches on generating depth distribution of atoms from peak shape analysis have been attempted. A brief review is presented herein. For experimental and calculation details please refer to original works.

3.2.1. Tougaard algorithm

A method for quantitative XPS which, by analysis of the peak shape, automatically accounts for the effect of variation in atomic concentration with depth was developed by Tougaard [29–31]. The method relies on a visual inspection of the agreement between the spectrum and a calculated background over a wide energy range. Recently, Tougaard proposed a simplified algorithm in which the background is adjusted to match the spectrum at a single energy below the peak [32]. Tougaard also has demonstrated the potential of the same method for quantitative and non-destructive imaging of the in-depth distribution of atoms, as well as of the amount of species at 3λ (where λ is the inelastic electron mean free path) in the outermost few nanometers, and therefore, the ability to produce 3D images [33,34]. The algorithm provides a criterion that can be used as a rough indication of the in-depth distribution of atoms, i.e. whether atoms are located at surface region (depth $< \lambda$), in the bulk (depth $> \lambda$) or homogeneously distributed throughout the depth.

This algorithm was applied to a multispectral XPS image data set acquired within the energy range of F 1s photoelectron peak (from 746.7 to 816.7 eV kinetic energy with a step size of 0.5 eV, and an 80 eV pass energy) from a sample consisting of a Teflon substrate with a patterned overlayer in the form of circular disks (called rods). The suggested thickness of the rods is 10 nm.

Each pixel within images contains a full F 1s spectrum. The peak structure of interest is centered on the energy E_p. A constant intensity, equal to that at energy $E_{\max}$ chosen 30 eV above the peak structure, is subtracted from the entire spectrum and the spectra are automatically analyzed using Tougaard's algorithm to produce several images [32].

The black points in Fig. 1a–c are those pixels where F atoms are at depths <1λ (surface), at depths >1λ (bulk) and where F atoms have a roughly constant concentration throughout the depth interval from 0 to 3λ (homogeneous), respectively. Some pixels in the center of the rods are not represented in any of the three figures. These correspond to pixels where the F atoms are all depths >3λ. From Fig. 1c it is concluded that F atoms are homogeneously distributed outside the region of the polymer rods and that the amount of F (within 3λ depth) is highest there, which is in agreement with expectations. No fluorine is seen in the center part of the polymer rods. This shows that the rod thickness is larger than 3λ (84A). There are some pixels around the rim of the rods where F atoms are located in the bulk. This is explained if the rods are not perfect cylinders, because the regions at the rim would then contain F atoms at depths between 1λ (28A) and 3λ (84A) while at the center, all pixels contain F atoms only at depths >3λ (84A). For a few other pixels around the rim of the rods, F atoms are located at the surface. This indicates segregation of F to the surface at the edge of the polymer rod.

It is important that all information about the distribution of atoms in the overlayer has been obtained by analyzing the spectra taken from the substrate atoms. It is possible to make a finer grid on depth criteria to make a better resolution for depth sectioning and thereby to get more detailed information on the uniformity of the contamination and the overlayer. Tougaard's algorithm gives both a more accurate image of the amount of substance and several images of depth distributions of atoms in the outermost few nanometers of the sample. This method, however, is limited to providing distribution of elements and not chemical species.

3.2.2. MVA/modeling inelastic background

Walton and Fairley have shown that by maintaining the relationship between images and spectra, it is possible to progress beyond the application of spectroscopic processing to multispectral imaging data sets, by utilizing the three-dimensional information contained in such data sets, to therefore improve both the processing and the visualization of the data [35]. They have modeled inelastic background of transmission corrected spectra to provide spatially resolved in-depth information.

A sample of this study was a failed metallization layer, consisting of silver deposited onto nickel overlying a titanium layer. The multispectral imaging data set consisting of 901 images, of 256 × 256 pixels, was acquired from 900 to 0 eV binding energy, in 1 eV steps, at 160 eV pass energy, equivalent to a resolution of 3.6 eV full width half maximum (FWHM), and with 5 s dwell time per image. The NIPALS procedure was used to compute the image abstract factors, following Poisson pre-filtering [36]. Data with better signal/noise were obtained by reconstructing the data sets using only the first six abstract factors. The images were then converted to spectra, and quantified by measuring photoelectron peak areas using a Shirley background, and theoretical sensitivity factors, at every pixel in the image, to produce atomic concentration images.

In order to visualize the spectra associated with different components in the image, the pixels in the second image abstract factor were classified in three regions. The spectra within each classification have been summed, and are colored according to their classification (Fig. 2). In this way, spectra from image regions where PCA-indicated different chemistry could be displayed. High back-

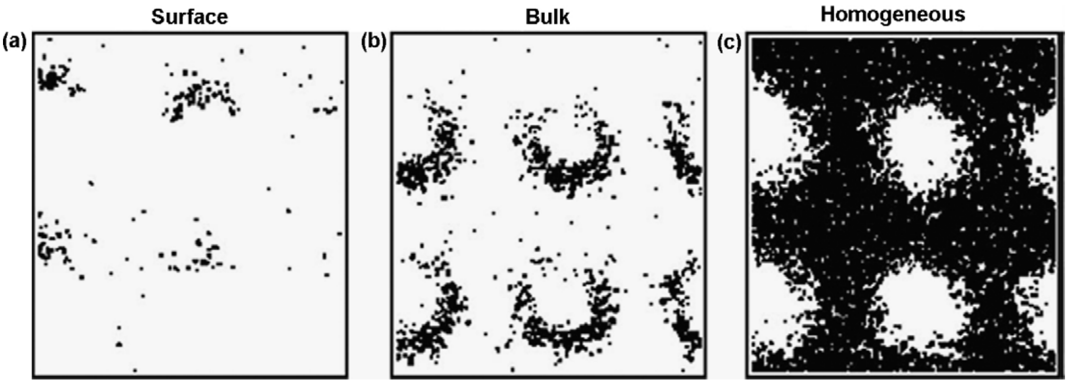

Fig. 1. (a) Image of pixels (black points) in which most F atoms are at depth less than 1λ. (b) Image of pixels (black points) in which most F atoms are at depth larger than 1λ. (c) Image of pixels (black points) in which F atoms are uniformly distributed in outermost 3λ. Reprinted from Hajati et al. [34] with permission from Wiley.

ground of the Ag 3d photoelectron peak can be seen to be associated with an increase in C 1s intensity from the overlayer contamination.

Since the data have been corrected for the intensity/energy response of the instrument, it is possible to model the inelastic background to obtain in-depth information. To obtain in-depth information from the failed metallization layer, the pixels in the nickel atomic concentration image have been classified by intensity, so that only regions rich in nickel are included in the summed spectra. The inelastic background has been modeled using the Quases [37] software package using the TPP-2M method to calculate the inelastic mean free path. This procedure utilizes a Tougaard description of the inelastic background, as described above. Modeling indicates an oxide thickness of 7.2 nm. Since this is much greater than that expected for an air-formed oxide, approximately 1 nm, it is further proof that failure occurred in the oxide layer.

Modeling the inelastic background to the mean spectrum allows the procedure to be undertaken interactively and without any assumptions as to the in-depth distribution. The analysis may be applied to the widescan spectrum acquired for quantification so that no further data need to be acquired.

In another example from Smith et al. multispectral images from the capping Germanium layer of a multilayer infrared optical filter have been quantified the same way as described above [38]. Quantified data were used to image the thickness of the oxide layer. The oxide thickness, d, can be calculated from:

$$d = L\ \cos\theta \ln\left(1 + \frac{R_{\text{exp}}}{R_0}\right) \tag{1}$$

where L is the virtually identical attenuation length of the Ge 3d electrons from the oxide and underlying metal (within the oxide), θ is the emission angle from the normal, R_{exp} is the measured Ge 3d intensity ratio $I_{\text{GeO}_2}/I_{\text{Ge}}$ from the sample, and R_0 is the same ratio for signals from infinite solids with flat surfaces measured under identical conditions.

Eq. (1) can be applied to the data in the Ge 3d oxide and metal images to generate the oxide thickness map shown in Fig. 3. From the thickness map, the spectra corresponding to any particular thickness of the oxide can be generated by selecting the pixels within the appropriate color range and summing their spectra. This approach is mostly useful for obtaining thicknesses of overlayers and does not provide distribution of chemical phases in 3D volume of material.

3.3. XPS mapping using automatic ARXPS

New instrumental capabilities were tested in mapping Si (1 0 0) wafers [39]. The XPS measurements were conducted in a Thermo VG Scientific Theta 300 instrument that records spectra over the range of emission angles simultaneously and which has a transition state to form maps of spectra. The ranges of 23–83° were split in 16 intervals, each of 3.75°. This provided 16 spectra of 112 energy channels from 90.77 to 110.23 eV binding energy at 0.1827 eV energy intervals for each point in the map. The map was formed by an array of 26 steps in the y-direction and 34 in the x-direction at 5.11 mm displacements. Fitting Si 2p spectra for each of angles gave a set of intensities of elemental and oxide peaks as a function of the emission angle, which was used to deduce the oxide thickness.

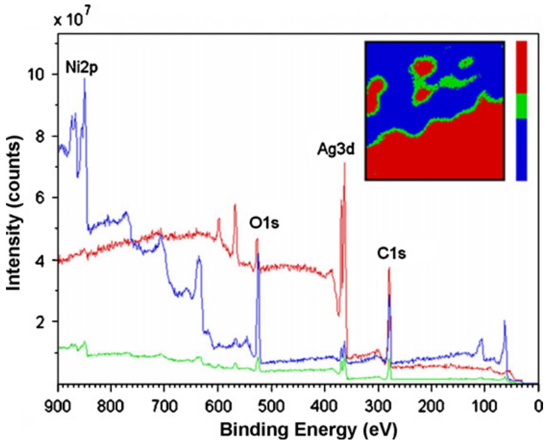

Fig. 2. Spectra summed from regions indicated in the false color image produced by pixel classification of the second image abstract factor (inset, 800 μm × 800 μm field of view). Upper region in the classified image is nickel rich, and the lower region silver rich. Reprinted from Walton and Fairley [35] with permission from Wiley.

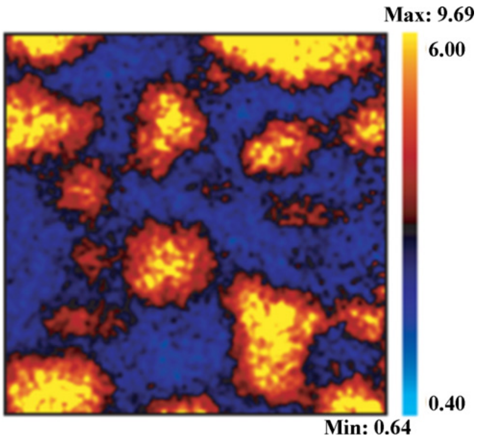

Fig. 3. Oxide thickness maps in bicolor. Reprinted from Smith et al. [38] with permission from Wiley.

Mapping of the SiO_2 thicknesses was done with good precision. It was concluded that when overlayer is of a uniform material, the most effective way of deriving the thickness is to use the data for all angles of emission up to 60° from the surface normal. The thickness data were calculated for each of the 10° in this range and then are averaged to give one d_{oxide} value at each pixel. A map of 884 mapping points was obtained with a thickness precision of 0.5% in 36 h of acquisition. Extending this method towards mapping of all elemental and chemical phases automatically at all angles presents an opportunity to build real 3D volume of materials.

3.4. 3D imaging using angle-resolved imaging

All of the methods discussed above provide indirect information that is related to 3D distribution of atoms at subsurface region. The next example will discuss a way to generate a real 3D volume of material from XPS images.

Recently, we have demonstrated an approach for combining ARXPS and imaging for analysis of 3D structure of heterogeneous samples [40]. As a result of the developed methodology, angle-resolved imaging data are visualization in 3D space, so that morphology within the top 3–10 nm of the polymer blend and the degree of surface segregation can be evaluated in detail.

Challenges in combining widely utilized angle-resolved spectroscopic analysis with imaging include locating the same area for image acquisition at multiple take-off angles, the small depth of focus in imaging mode, and the geometrical transformation of images with changing take-off angle. The conversion of the original photoelectron images to a volume representing the top 3–10 nm of the polymer blend requires spatial image transformation to correct for geometry or image warping, automatic image registration, mapping images to concentration with the assistance of AR small area spectroscopy, image morphing and visualization. Due to the difference in depth of focus between imaging and spectroscopic modes of the analyzer, small area spectra provide composition from slightly different depths than images. Therefore, the constructed 3D volumes of material represent semiquantitative results, from which relative rather than absolute compositions can be discerned.

We have used samples of polyvinylchloride (PVC) and polymethylmethacrylate (PMMA) blend, which are heterogeneous both laterally and vertically, as test system. Images and small area spectra from selected areas within images were acquired at TOAs of 90°, 60°, 45°, 30° and 15°. A grid was placed on top of the sample to be used for image registration purposes. Fig. 4 shows the Cl 2p, representative of the PVC-enriched phases, and associated background images for take-off angles of 90°, 60° and 30°. Cl 2p images were used to visualize 3D morphology of the PVC-enriched areas of the blend.

As the first step towards unimodal visualization of the angle-resolved imaging data, the tilted images (60°, 45°, 30° and 15° TOA) were registered with the image acquired at a 90° TOA. The type of spatial transformation that can describe the relationship between images at different TOAs is *projective*. It allows angular and length distortion, thus allowing the rectangle to be transformed into an irregular quadrilateral. It does not preserve parallelism, while linearity is maintained.

Image registration is broken down into two steps. First, the orientation of the sample with respect to the analyzer is corrected by projective spatial transformation of the images using control point selected manually on background images capturing rectangular grid opening. The transformed or *warped* images are then brought to the best match between each other using automatic image registration (AIR) using rigid *linear* transformation of translation and rotation. AIR iteratively adjusts spatial transformation parameters so as to maximize a similarity measure (mutual information in this case) computed between the transformed target image and the corresponding reference image [41,42].

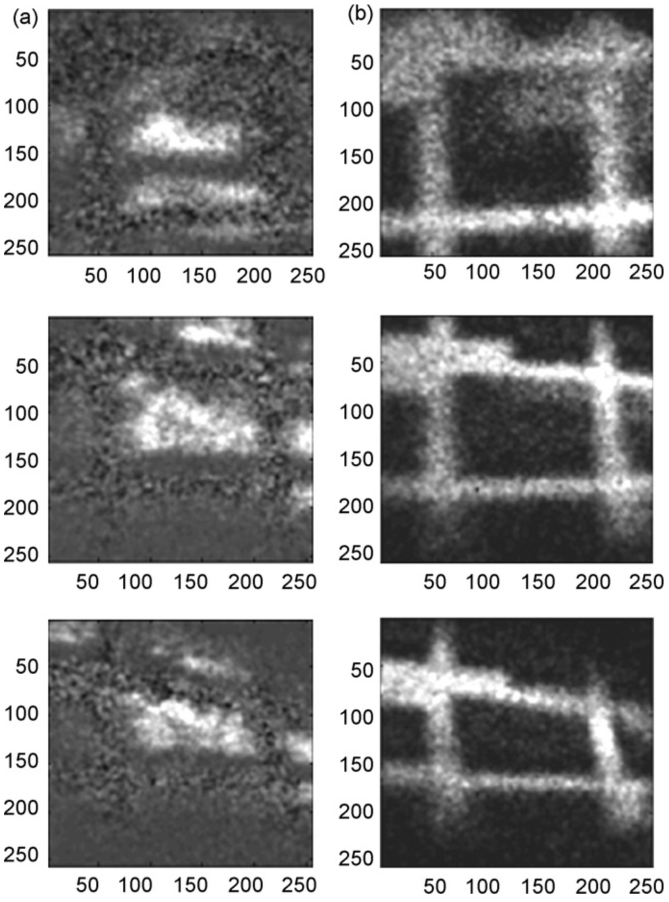

Fig. 4. 700 µm × 700 µm Cl 2p (a) and associated background (b) images for 90° (top), 60° (middle) and 30° (bottom) TOAs. Background images reflect the changes in geometry which occur when tilting the sample. Reprinted from Artyushkova and Fulghum [40] with permission from Elsevier.

Fig. 5 shows the resulting registered Cl 2p images representing polymer separation at different TOAs and therefore at different depths. The large feature in the center of the Cl 2p image at 30° TOA decreases in size with increasing depth, and new features appear in deeper layers. The images in Fig. 5 are a qualitative representation of polymer blends at various depths near the surface. In order to convert these images into a quantitative representation, concentration mapping is required. 55 µm diameter C 1s spectra from high and low intensity areas within the Cl 2p images at all TOAs were curve fit using model photopeaks of PVC and PMMA [43]. The intensities in the original registered images (counts per second) were mapped to PVC concentration based on the small area analyses. The result of this mapping is semiquantitative as absolute values of concentrations obtained from small area spectroscopy will come from slightly different sampling depths than images due to difference in acceptance angle in spectroscopic and imaging modes of the instrument. Relative trends in composition in lateral and vertical dimensions, however, can be evaluated using this approach, quite reliably.

The next step towards 3D visualization requires merging the information from all of the quantitative images, representing the PVC-enriched phase at different depths, into one display. However in real heterogeneous samples, where surface segregation may exist, pixels belonging to the same feature in one slice do not necessarily connect to pixels exactly beneath them in the next slice. There are several ways to address this correspondence problem. An example of one such approach is *image morphing*. The morphing is

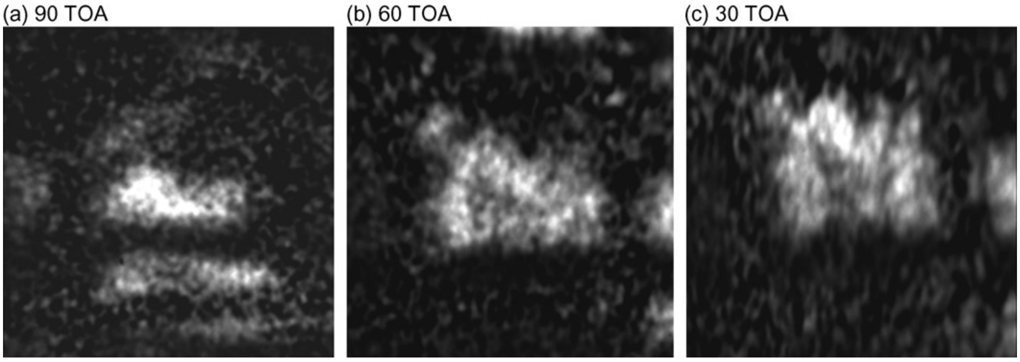

Fig. 5. Registered main peak Cl 2p images at (a) 90°, (b) 60° and (c) 30° TOAs. Reprinted from Artyushkova and Fulghum [40] with permission from Elsevier.

realized by coupling image warping (interpolation of shape) with color interpolation. Image warping applies 2D geometric transformations to the images in order to retain geometric alignment between their features, while color interpolation blends their color to produce in-between images [44].

As the images at different TOAs are not equally spaced, different numbers of intermediate slices must be created between each consecutive pair. The approximate depths of the images are assumed to be 10, 8.6, 7, 5 and 2.6 nm at 90°, 60°, 45°, 30° and 15°, respectively. This approximation is a simplistic attempt to take into account exponential attenuation of the photoelectron signal. To create a set of equally spaced slices, a step of 0.2 nm was chosen and 7, 8, 10 and 12 slices were created using morphing between 90° and 60°, 60° and 45°, 45° and 30°, 30° and 15° image pairs, respectively. This approach results in a total of 42 slices representing approximately the top 10 nm of the polymer blend surface. The images created by morphing, in combination with the processed XPS images, are stacked into a volume and visualized within our GUI *Volumization*, written in Matlab [45,46]. Fig. 6 shows 3D visualization of PVC-enriched phase. A whole volume can be rendered and the transparency can be adjusted to represent the inside or outside of the material (Fig. 6a). Different color schemes can be selected to visualize the change in concentration from the top to the bottom. The orthogonal cross-sections can be displayed to see the inside of the material at various planes (Fig. 6b). The isosurface is the most useful, as it connects all the points within the 3D volume having the same concentration of the phase visualized. This allows for quantitative interpretation of the images. The single isosurface for a polymer blend composition of 5%PVC/95%PMMA is displayed in Fig. 6c. Multiple isosurfaces can be displayed as well. Fig. 6d shows three isosurfaces representing three different compositions of the blend, i.e. 5/95, 12/88 and 22/78. The separation of the phase with depth is evident from this display.

This approach provides real 3D volumes of the material within top 10 nm, but it should be applied with understanding of its limitations. Small depth of focus in imaging mode causes large height differences between upper and lower parts of the image, especially at the very shallow angles. Only narrow part in the middle of images can be usefully combined into a volume. Moreover, merging of features at shallow depths due to the tilt of the sample and small depth of focus may be misinterpreted as real morphological changes. To identify part of the images that are in focus and to evaluate minimum distance between features that can still be resolved while the

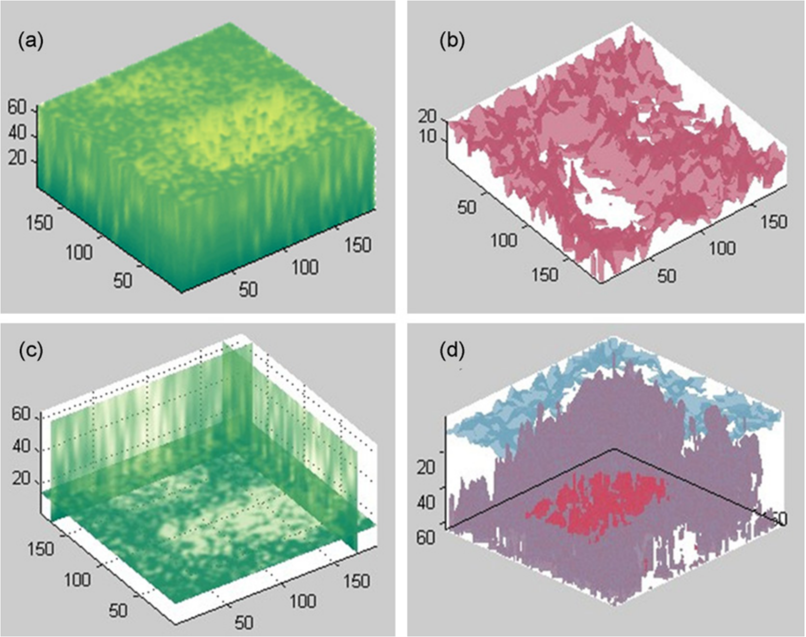

Fig. 6. Volume visualization of the three-dimensional volume representing the PVC-enriched phase of the polymer blend: (a) the whole volume rendered, (b) three orthogonal slices showing the interior of the volume, (c) single isosurface showing 5/95 PVC/PMMA composition of the blend and (d) multiple isosurfaces displaying three compositions 5/95, 12/88 and 22/78 of the blend. Reprinted from Artyushkova and Fulghum [40] with permission from Elsevier.

Table 1
ARXPS quantitative results.

	283.9	284.6	285.2	286.4	287.5	288.5	289.4	530.9	531.6	532.2	533.2	N 1s
1L	0.0	41.6	20.0	5.0		6.0		8.6		16.5	0.8	1.50
1L 40	0.0	42.6	21.7	4.2		5.8		7.8		15.3	1.1	1.60
1L 55	2.8	43.7	20.6	4.9		4.7		4.3		15.9	1.5	1.55
1L 65	5.0	43.6	19.4	4.8		4.1		4.5		15.5	1.7	1.40
1L 75	10.3	41.1	20.2	3.1	1.3	2.9		4.3		14.5	0.8	1.51
2L	0.0	32.0	18.7	8.4	1.5	5.8		4.0	1.5	20.5	4.2	3.5
2L 40	0.0	36.3	14.9	7.8	3.8	4.3		4.5	5.8	17.4	2.1	3.1
2L 55	6.9	28.0	18.5	9.8	2.9	3.4		4.5	3.8	15.1	4.1	2.9
2L 65	7.2	27.0	23.4	6.7	2.7	2.9		3.9	5.5	14.0	3.8	2.9
2L 75	9.9	28.8	23.4	5.1	2.6	2.5		3.2	5.6	13.3	2.6	2.8
3L	0.0	44.3	18.0	7.9	1.5	2.8		1.6	3.2	14.0	1.7	5.0
3L 40	7.4	41.7	15.8	7.1	1.7	2.8		1.1	3.4	13.4	2.2	3.4
3L 55	7.8	36.3	22.6	5.6	1.7	2.2		2.1	1.4	15.4	2.0	3.0
3L 65	18.3	39.7	9.0	8.1	0.3	2.3		4.2	2.0	11.9	1.1	3.2
3L 75	17.0	29.6	24.9	6.4	1.3	2.3		0.8	5.2	9.6	0.0	3.0
4L	0.0	38.3	14.3	11.9	3.4	3.4	0.0	2.2	10.1	7.4	3.2	5.7
4L 40	5.4	33.8	19.0	8.9	2.3	3.3	0.5	0.5	7.9	10.9	2.7	4.8
4L 55	12.1	32.2	18.4	5.9	2.1	2.2	0.4	1.6	6.8	12.5	2.1	3.7
4L 65	12.2	32.1	21.4	5.2	1.6	1.8	0.3	1.7	7.1	12.5	2.0	2.4
4L 75	15.8	17.9	29.0	5.3	1.7	1.2	1.1	0.4	3.2	12.2	10.1	2.2

sample is tilted, grids with various sizes of mesh may be imaged at the same time as real samples.

3.5. 3D analysis using PARAFAC applied to ARXPS data

In this example, the physical architecture of ultra thin bilirubin *oxidase* (BOD) films created via layer-by-layer deposition, including elemental and chemical composition, relative thickness and assembly of layers, has been investigated in detail by ARXPS [47]. A multilayer architecture, which contains ordered layers of BOD, was assembled by means of alternate electrostatic adsorption with positively charged poly(ethylenimine) (PEI). The PEI forms a positively charged electrostatic layer on the negatively charged pre-adsorbed BOD layer. The PEI/BOD/C modified electrode was regarded as one layer of multilayer films modified carbon electrode (layer one). The additional layers of multilayer films modified carbon electrode were assembled by repeating the process of step 1 ($n-1$) times. This method of enzyme immobilization forms large three-dimensional multilayer structures of BOD–PEI complexes which promotes the preservation of the catalytic activity of immobilized BOD in solution and in the dehydrated state. The survey of each area is done first, followed by the recording of high-resolution spectra of C 1s, O 1s and N 1s for all the samples. ARXPS analysis of organic materials requires use of charge neutralizer, which causes degradation of angular resolution due to the use of magnetic lens. To avoid angular overlap, limited number of TOAs at large degree intervals is used for this analysis [48]. The following take-off angles (TOA) are selected for angle-resolved studies: 90°, 50°, 35°, 25° and 15°.

Table 1 shows the results of curve fit of C and O spectra for five samples (1L through 4L) for five TOAs. An increase of %N with an increase of number of bi-layers manifests the layer growth. High-resolution C 1s spectra for layer by-layer samples have a substantial peak at 288.5 eV coming from BOD, which is larger for deeper sampling depths for all samples, confirming BOD as being a first deposited layer for all samples. This peak is decreased with an increase of the number of BOD/PEI bi-layers. This decrease may be caused by expected attenuation of the signal from BOD by the top PEI layer, but also by a chemical shift of unique peak of BOD due to interaction between PEI and BOD.

All layer-by-layer samples have the same unique peak that is only present in CE + PEI sample (results are not shown), which we have attributed to an interaction between the CE and PEI mainly [47]. Existence of this peak, thus, for layer-by-layer samples, indicates non-uniform coverage of BOD on a rough (tens of microns) carbon electrode surface. It may indicate that part of the CE surface is coming in contact with the PEI layer, which interacts with aldehyde groups directly on the CE surface. ARXPS data confirm the formation of ultrathin layer-by-layer architectures, where BOD is the first and PEI is the second part of a bi-layered structure. Importantly, layers are not discrete, but rather some intermixing of layers occurs.

Unique peaks of BOD at 288.5 eV and of CE at 284.6 eV were used in a substrate overlayer model for estimation of the relative thickness of the first layer of BOD on the carbon electrode surface [49]. At the same time, there is a challenge to estimate the PEI thickness on BOD using the same approach. Even though PEI has a unique peak at 285.4 eV, both BOD and CE also contribute to this part of the C 1s spectrum. The peak at 287.5 eV, being a unique peak due to an interaction component, may be used in an attempt to get relative values of PEI thickness on BOD. The values of thicknesses of BOD and PEI obtained can only be used for relative comparison between samples. The thicknesses of layers calculated via the substrate/overlayer model using the 288.5 eV peak for BOD, the 284.6 eV peak for CE and the 287.5 eV peak for PEI are shown in Table 2.

Data in Table 1 represent a three-dimensional matrix with three modes (variables) of depth (TOA), number of layers (sample) and chemical moiety (photoelectron peak). Parallel Factor Analysis (PARAFAC), which is a generalization of Principal Component Analysis (PCA) to higher order arrays, can be applied to this 3D data set to extract chemical and depth information for this multilayered samples. PARAFAC is a bi-linear decomposition method, which decomposes the array into sets of scores and loadings [50,51]. A 2-component model was constructed. Score plots of PC2 versus PC1 for three modes (TOA, number of layers and chemical species) are shown in Fig. 7a–c).

Score plot for TOA mode (Fig. 7b) shows alignment of TOAs along the second diagonal indicating that PC1 increases with decreasing sampling depth, while PC2 increases with increasing sample depth. For monotonically increasing thickness of layers from sample L1 to

Table 2
Overall relative thickness of BOD and PEI layers determined from overlayer model.

	BOD thickness on CE, nm	PEI thickness on BOD, 287.5, nm
L1	0.13	0.26
L2	0.30	0.74
L3	0.21	0.35

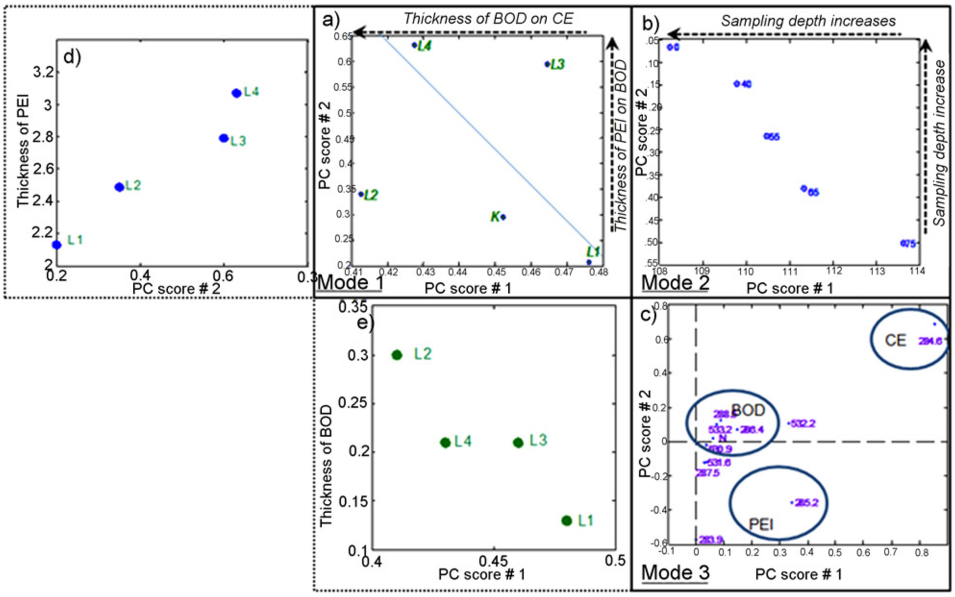

Fig. 7. PARAFAC 2-component model. Biplot for (a) sample mode, (b) TOA mode and (c) chemical species mode, (d) PC score #2 versus thickness of PEI and (e) PC score #1 versus thickness of BOD.

L4 one would expect the samples also to align along the second diagonal in Fig. 7a. However, only samples L1 and L4 fall onto the diagonal. In order to understand the relationship between samples as they are displayed on score plot (Fig. 7a), PC scores #1 and 2 are plotted against thickness of BOD (Fig. 7e) and PEI (Fig. 7d), respectively. A linear relationship is observed from these plots, indicating that PC1 represents distribution of samples according to thickness of BOD layer and PC2 separates samples and species by thickness of PEI layer on top of BOD. Thickness of PEI grows linearly with increase number of layers from sample L1 to L4, while thickness of BOD does not follow the same increase with number of deposited layers. The thickness of BOD increases from sample L1 to L2 but then decreases for L3 sample and stay the same for L4, indicating that bi-layered structure seems to get collapsed as number of bi-layers is larger than 2. Score plot for chemical species (Fig. 7c) confirms the chemistry of the multilayered structure where peaks due to CE are more significant for deeper depths, while peaks due to PEI is mostly significant for shallower depth with peaks due to BOD being in between.

This example shows how PARAFAC can be used to extract 3D information on multilayered samples from spectroscopic analysis. Similarly, PARAFAC or other multidimensional MVA methods can be applied to visualize chemistry in three dimensions from imaging XPS data sets, generated either through depth sputtering or angle-resolved images.

3.6. Comparison of methods

Ideally, the analyst would have a complete understanding of chemical and morphological structures of nanocomposites if quantitative 3D volumes of elemental and chemical phases at high spatial and vertical resolution could be provided non-destructively. None of the approaches discussed above can serve this goal. The main advantage of XPS in comparison with other imaging surface sensitive techniques is that it readily provides *quantitative chemical* information. Advantages and drawbacks of each of the methods discussed above in attempt to provide 3D structure of materials should be judged in this context as summarized in Table 3. Combination of imaging and sputtering represents the best fit to the ultimate goal of 3D imaging and is discussed below.

4. Future directions

4.1. Multivariate analysis of 3D imaging data

When multispectral images are acquired at each sputtered depth, four-dimensional data sets can result with full spectrum acquired at each voxel of the space. These data sets represent huge amount of data which can only be interpreted with assistance of multivariate analysis [14,18,19].

Table 3
Properties of 3D information provided by approaches discussed.

	Conventional image acquisition	Peak shape analysis	Modeling inelastic background	ARXPS mapping	AR imaging	ARXPS PARAFAC	Polyatomic sputtering/imaging
Elemental info	Yes	Yes	Yes	Yes	Yes	Yes	Yes
Chemical info	Yes	No	Limited	Yes	Yes	Yes	Yes
Quantification	No	Yes	Yes	Yes	Semi	Semi	Yes
Real 3D imaging	Yes	No	No	Yes, <10 nm	Yes, <10 nm	Yes w/images	Yes, much deeper
Thickness	Yes	Yes	Yes	Yes	Yes	Relative	Yes
Layered structures	Yes	Yes	Yes	Yes	Yes	Yes	Yes
Destruction	Yes	No	No	No	No	No	Removal of material with preserved chemistry
Overall understanding of chemistry and morphology with depth	No	Limited	Limited	Limited	Yes	Yes	Yes, w/MVA

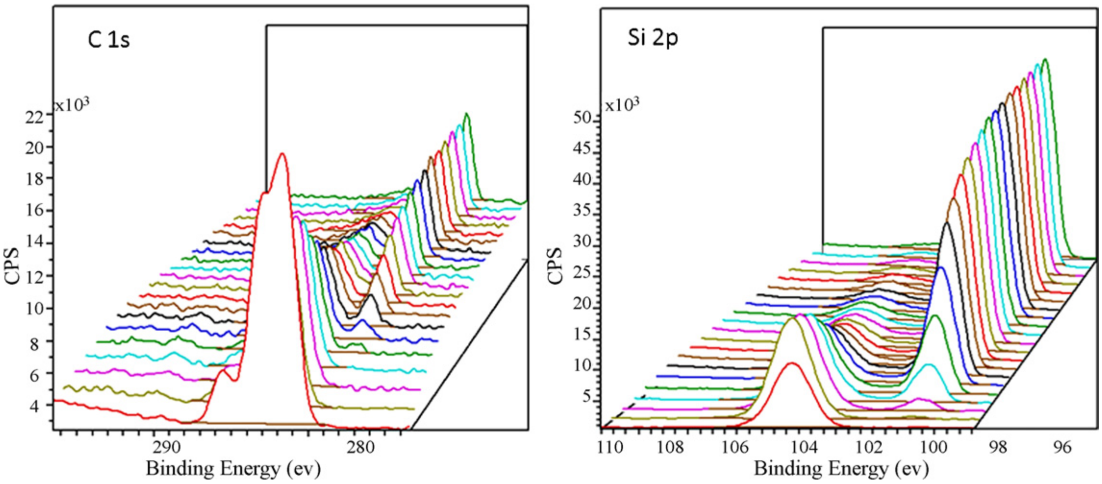

Fig. 8. C 1s and Si 2p acquired from yeast cells encapsulated in lipid/silica nanocomposite as a function of etch time using novel Coronene gun developed by Kratos.

There are several approaches that can be undertaken in extracting 3D chemical information from these data sets with assistance of Multivariate Analysis Tools. Multispectral images at each depth can be analyzed individually by preferred method of choice, such as PCA or MCR-ALS, to extract component images representing chemical phases present at each depth layer. The component images extracted from MSA, which show the spatial distribution of the various chemical components, can be stacked into volumetric data and visualized individually or together representing an overall chemistry of individual layers. If there are significant changes in chemistry however with depth, chemical components extracted from multispectral data at each layer might be different; so care should be taken in combining them into 3D stacks.

Another approach is two-step PCA and MCR analysis. The order of the variables has to be chosen first. Spectral sequences can be first analyzed by PCA/MCR for each fixed sputtered depth to provide spectral components and associated 3D score/component image sequences as discussed in previous paragraph. These 3D component image sequences correspond to the 3D spatial distribution of each spectral profile. Second, the previously computed 3D component image sequences are considered as conventional 3D image sequences and are analyzed by PCA/MCR at the second step. Alternatively, the depth sequences for each fixed BE can be analyzed by PCA/MCR at the first step to provide depth components and associated spectral score/component image sequences. These 3D component image sequences correspond to BE distribution at each depth. Second, the previously computed BE component image sequences are analyzed by PCA/MCR at the second step.

The most promising method is PARAFAC which was discussed above for analysis of 3D ARXPS data (Section 3.5). For four-dimensional data sets, containing a series of spectral images for each sputtered depth, the 4D array $[X \times Y \times Z \times R]$ may be unfolded into a three-way array $[XY \times Z \times R]$ (images are being unfolded into rows) analyzed with PARAFAC. The PARAFAC loadings in the BE and depth modes will describe the general changes of chemistry with depth while the loadings in the pixel dimension describe changes in specific pixels on the images. The output from PARAFAC presents very clear visualization of chemical, horizontal and vertical heterogeneities of samples. *Graphical User Interface for Multivariate Analysis of 4-Dimensional Data* [52] utilizing these approaches has been developed based on PLS_Toolbox 5.0 for Matlab [53].

4.2. Polyatomic guns for analysis of biological soft samples

Recent introduction of cluster ion beams, such as C60 and Coronene, into XPS instrumentation offers capabilities in quantifying the chemical and molecular gradients in the near surface region of soft materials, such as polymers and biomaterials. XPS data can be acquired as a function of sputter depth into organic materials while maintaining molecular integrity [28].

We have recently attempted to study the interface between 5 μm yeast cells encased in a phosphatidylcholine lipid/silica nanostructure using a novel Coronene gun developed by Kratos [54]. Fig. 8 shows C 1s and Si 2p spectra as a function of sputtering time. Spectra obtained demonstrate rich chemical information without evidence of damage. An initial photoelectron signature of

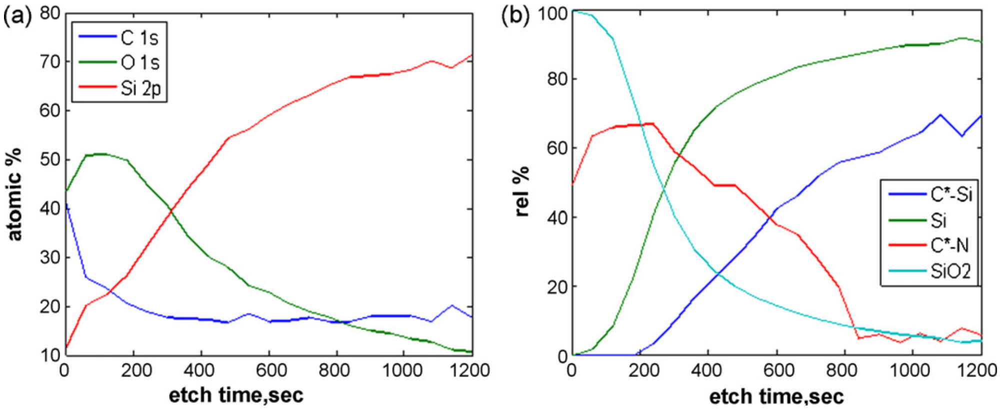

Fig. 9. Depth profile generated shown as a function of etching time: (a) elemental composition and (b) speciation.

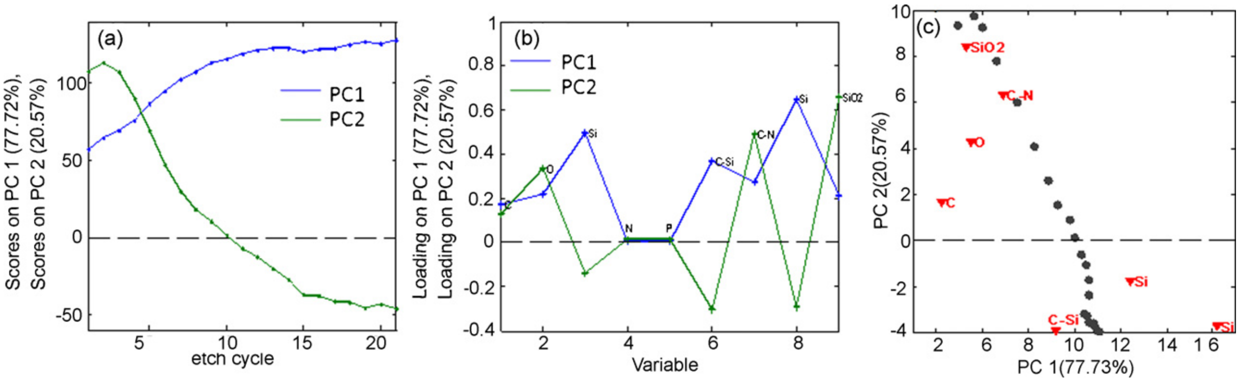

Fig. 10. PCA results applied to elemental and chemical composition as a function of sputtering time: (a) loading plot, (b) score plot and (c) biplot.

cells encased in lipids disappearing with depth, and new peak at lower BE due to silica-carbide increases as the gun sputters through silica support.

At the same time, SiO_2 which is present at 10% at the very top of the sample changes towards metallic Si. Fig. 9 shows depth profiles reconstructed for C 1s, O 1s and Si 2p as well as two types of C and Si that have been obtained from curve fitting. At ~800 s, all N and P is removed (not shown) and the composition reaches that of silicon with some Si–C species. At the cell–air interface SiO_2 is detected along with C–N species. At ~300 s of sputtering the interface between cells and lipid is reached which is manifested by decrease in C–N and formation of C–Si bond. This confirms hypothesis that cells are being covered with Si.

Principal Component Analysis was applied to XPS quantitative results combining elemental and chemical species as a function of etch time. Fig. 10 plots score and loadings as well as biplot for 2-component model extracted. The first component which is increasing with depth has dominating contribution from Si in form of metallic Si as well as C–Si species. The second component which is increasing with larger speed has large contribution due to C–N and SiO_2. Biplot shows even clearer distribution of species as a function of sputtering depth. SiO_2 is located slightly above C–N type of N indicating encapsulation of cells. At cycle #9, contribution of carbide becomes important which might be at interface between lipid and Si substrate. At the end of sputtering metallic Si dominates composition.

This experiment possible only with a new type of cluster sources for sputtering provides insight into the mechanism of cell-directed assembly. One can envision extending similar experiment and multivariate analysis to 3D imaging of biologically relevant materials.

Acknowledgements

The XPS was funded by a grant from the Keck Foundation and UNM. We would like to thank Kratos for acquiring depth profiling data using a novel Coronene gun.

References

[1] V.A. Ignatova, S. Van den Berghe, S. Van Dyck, V.N. Popok, Microscopy and Microanalysis 12 (5) (2006) 432–437.
[2] H. Kato, K. Nishizaki, K. Takahashi, H. Nohira, N. Tamura, K. Hikazutani, S. Sano, T. Hattori, Applied Surface Science 190 (1–4) (2002) 39–42.
[3] T. Nakano, S. Sato, S. Baba, Vacuum 74 (3–4) (2004) 591–594.
[4] S.R. Sheng, H.Y. Hao, H.W. Diao, X.B. Zeng, Y. Xu, X.B. Liao, T.L. Monchesky, Applied Surface Science 253 (3) (2006) 1677–1682.
[5] A. Delcorte, Applied Surface Science 255 (4) (2008) 954–958.
[6] A. Wucher, J. Cheng, N. Winograd, Analytical Chemistry 79 (15) (2007) 5529–5539.
[7] J. Cheng, A. Wucher, N. Winograd, Journal of Physical Chemistry B 110 (16) (2006) 8329–8336.
[8] E.A. Jones, N.P. Lockyer, J.C. Vickerman, Analytical Chemistry 80 (6) (2008) 2125–2132.
[9] H. Nygren, B. Hagenhoff, P. Malmberg, M. Nilsson, K. Richter, Microscopy Research and Technique 70 (11) (2007) 969–974.
[10] A. Wucher, Applied Surface Science 252 (19) (2006) 6482–6489.
[11] L.L. Zheng, A. Wucher, N. Winograd, Analytical Chemistry 80 (19) (2008) 7363–7371.
[12] P.G. Kotula, M.R. Keenan, J.R. Michael, Microscopy and Microanalysis 12 (1) (2006) 36–48.
[13] J.X. Gao, E. Liu, D.L. Butler, A.P. Zeng, Surface & Coatings Technology 176 (1) (2003) 93–102.
[14] K. Artyushkova, J.E. Fulghum, Surface and Interface Analysis 33 (3) (2002) 185–195.
[15] D.E. Peebles, J.A. Ohlhausen, P.G. Kotula, S. Hutton, C. Blomfield, Journal of Vacuum Science & Technology A 22 (4) (2004) 1579–1586.
[16] U. Vohrer, C. Blomfield, S. Page, A. Roberts, Applied Surface Science 252 (1) (2005) 61–65.
[17] J. Walton, N. Fairley, Surface and Interface Analysis 36 (1) (2004) 89–91.
[18] A. Hoskuldsson, K.H. Esbensen, Journal of Chemometrics 17 (1) (2003) 45–52.
[19] E.R. Malinowski, Factor Analysis in Chemistry, Wiley, New York, 1991.
[20] T.G. Lee, J.W. Park, H.K. Shon, D.W. Moon, W.W. Choi, K. Li, J. Chung, Applied Surface Science 255 (2008) 1241–1248.
[21] Theta Probe—High Performance ARXPS Spectrometer. http://www.thermo.com.
[22] JPS-9200 Photoelectron Spectrometer (ESCA). http://www.jeol.com/PRODUCTS/ElectronOptics/SurfaceAnalysisSA/tabid/95/Default.aspx.
[23] PHI Quantera XPS Microprobe. http://www.phi.com/products/quantera/overview.html.
[24] Axis Ultra DLD. http://www.kratosanalytical.net/surface/.
[25] ESCALAB 250. www.thermo.com.
[26] NanoESCA, 2007.
[27] Sputter Depth Profiling Organic Films with the PHI 06-C60 Sputter Ion Gun, Physical Electronics, Inc., USA 2006.
[28] A. Rafati, A.G. Shard, M.R. Alexander, M.C. Davies, NMAET III & SSBII 10 Meeting, Teddington, UK, 2008.
[29] S. Tougaard, Applied Surface Science 100–101 (1996) 1–10.
[30] S. Tougaard, Surface and Interface Analysis 26 (4) (1998) 249–269.
[31] S. Tougaard, H.S. Hansen, Surface and Interface Analysis 14 (11) (1989) 730–738.
[32] S. Tougaard, Journal of Vacuum Science and Technology A 21 (4) (2003) 1081–1086.
[33] S. Hajati, S. Coultas, C. Blomfield, S. Tougaard, Surface Science 600 (15) (2006) 3015–3021.
[34] S. Hajati, S. Coultas, C. Blomfield, S. Tougaard, Surface and Interface Analysis 40 (3–4) (2008) 688–691.
[35] J. Walton, N. Fairley, Surface and Interface Analysis 40 (3–4) (2008) 478–481.
[36] J. Walton, N. Fairley, Journal of Electron Spectroscopy and Related Phenomena 148 (1) (2005) 29–40.
[37] S. Tougaard, Quases. www.quases.com/.
[38] E.F. Smith, D. Briggs, N. Fairley, Surface and Interface Analysis 38 (2) (2006) 69–75.
[39] M.P. Seah, R. White, Surface and Interface Analysis 33 (2002) 960–963.
[40] K. Artyushkova, J.E. Fulghum, Journal of Electron Spectroscopy and Related Phenomena 149 (1–3) (2005) 51–60.
[41] K.J. Black, T.O. Videen, J.S. Perlmutter, Journal of Computer Assisted Tomography 20 (5) (1996) 855–861.
[42] B. Zitova, J. Flusser, Image and Vision Computing 21 (11) (2003) 977–1000.
[43] K. Artyushkova, J.E. Fulghum, Surface and Interface Analysis 31 (5) (2001) 352–361.
[44] G. Wolberg, Visual Computer 14 (8–9) (1998) 360–372.
[45] K. Artyushkova, software for Matlab, GUI got Visualizing 3D images, http://www.mathworks.com/matlabcentral/fileexchange/.
[46] The MathWorks, I. *MatlabR2007*, Natick, Massachusetts, 1998.

[47] D. Ivnitski, K. Artyushkova, P. Atanassov, Bioelectrochemistry 74 (1) (2008) 101–110.
[48] P. Cumpson, Journal of Electron Spectroscopy and Related Phenomena 73 (1) (1995) 25–52.
[49] P. Cumpson, ARCtick. http://www.npl.co.uk/server.php?show=ConWebDoc.607.
[50] R. Bro, Chemometrics and Intelligent Laboratory Systems, vol. 38, 1997, pp. 149–171.
[51] R.A. Harshman, M.E. Lundy, Computational Statistics & Data Analysis 18 (1) (1994) 39–72.
[52] K. Artyushkova, software for Matlab, GUI for Multivariate Image Analysis of 4-dimenional Data, http://www.mathworks.com/matlabcentral/fileexchange/.
[53] Eigenvector Research Inc. PLS_Toolbox 5.2, 2008.
[54] Kratos Analytical. http://www.kratosanalytical.net/surface/.